Twin-enhanced magnetic torque

Anthony Hobza[1*], Carlos J. García-Cervera[2], Peter Müllner[1†]
[1]Micron School of Materials Science and Engineering, Boise State University, Boise, ID 83725
[2]Department of Mathematics, University of California, Santa Barbara, CA 93106

Abstract

Magnetic shape memory alloys experience magnetic-field-induced torque due to magnetocrystalline anisotropy and shape anisotropy. In a homogeneous magnetic field, torque results in bending of long samples. This study investigates the torque on a single crystal of Ni-Mn-Ga magnetic shape memory alloy constrained with respect to bending in an external magnetic field. The dependence of the torque on external magnetic field magnitude, strain, and twin boundary structure was studied experimentally and with computer simulations. With increasing magnetic field, the torque increased until it reached a maximum near 700 mT. Above 200 mT, the torque was not symmetric about the equilibrium orientation for a sample with one twin boundary. The torque on two specimen with equal strain but different twin boundary structures varied systematically with the spatial arrangement of crystallographic twins. Numerical simulations show that twin boundaries suppress the formation of 180° domains if the direction of easy magnetization between two twin boundaries is parallel to a free surface and the magnetic field is perpendicular to that surface. For a particular twin microstructure, the torque decreases with increasing strain by a factor of six due to the mutual compensation of magnetocrystalline and shape anisotropy. When free rotation is suppressed such as in transducers of magneto-mechanical actuators, magnetic-field-induced torque creates strong bending forces, which may cause friction and failure under cyclic loading.

I. INTRODUCTION

As all magnets do, magnetic shape memory alloy (MSMA) samples experience a torque when exposed to a magnetic field that is not parallel to the magnetization of the sample. Although very basic, this torque has been neglected in almost the entire literature on the magneto-mechanics of MSMAs as exemplified in a recent review[1]. Zheng *et al.*[2] demonstrated magnetic-torque-induced bending (MTIB) of MSMA wires and Kucza *et al.*[3] discovered a shape effect according to which long samples (i.e. samples with a large length-to-width aspect ratio) deform in a magnetic field mostly by bending (i.e. MTIB) while short samples (i.e. samples with a small aspect ratio) deform axially by magnetic-field-induced straining (MFIS).

MFIS proceeds by deformation twinning in the low temperature martensite phase. Twin boundaries move if the stress induced by an external magnetic field exceeds a critical stress referred to as the twinning stress. Twin boundary motion reorients the anisotropic unit cell. As the twin boundary moves through the material, one twin domain grows and the other shrinks, which results in a macroscopic shape change. The driving force for twin boundary motion in an external field has been analytically described as the change in magnetic energy over a finite distance the twin boundary moves[4-6]. The authors applied micromagnetic principles in their energy calculations. In analytical methods, many

* Now at SpaceX, Rocket Road, Hawthorne, California
† Corresponding author: petermullner@boisestate.edu

times only the external field and magnetocrystalline anisotropy energies are accounted for[5,7,8]. Typically, authors assume that a twin domain is homogeneously magnetized[5,9,10], which ignores the potential for 180° domain walls to form. Other models, which include 180° magnetic domains, fix domain fractions such that the 180° magnetic domain wall maintains continuity across the twin boundary[11,12].

These models differ from experimental findings of Lai *et al.* who described that 180° domains existed in the twin domain with axis of easy magnetization perpendicular to the external field[13]. The 180° domain walls did not maintain continuity at a twin boundary. Analytical calculations were based on a physical model of the magnetic structure in the material. The assumptions taken to create the physical model restricted the energy landscape the model can access. The validity of the physical model was not re-assessed once the energy minimization was completed. The complexity of magnetic and mechanical microstructures made it nearly impossible to create a reasonable model to describe the material. In the case of a bending sample[2,3,14], the axis of easy magnetization is not simply parallel to or perpendicular to the magnetic field. Additionally, the twin structure changes depending on the amount of bending, and twin boundaries may not be parallel.

Magnetic field induced bending in magnetic shape memory alloys was reported on a thin film and attributed to a magnetic field gradient in an inhomogeneous field[14]. The authors noted that, even in a homogeneous field, the magnetocrystalline and shape anisotropy result in a torque on the specimen. Zheng *et al.* first reported on bending in a homogeneous magnetic field[2]. The authors rotated an oligocrystalline wire in a homogeneous field; the wire not only experienced axial strain but also magnetic-torque-induced bending. The driving force for bending was attributed to magnetic torque; twin boundary motion accommodated bending. Kucza *et al.* further studied MTIB in a homogeneous field by rotating single crystal specimen with varying aspect ratio in an external magnetic field[3]. The bending strain increased with increasing aspect ratio, while the axial strain stayed consistent. The authors qualitatively described the torque magnitude in terms of the Zeeman, magneto crystalline and shape anisotropy energies. The authors discussed the influence of magnetic energies on the dependence of bending on the external magnetic field and sample geometry[3]. However, a bending specimen presents an exceptionally difficult system to analyze quantitatively. Many twin boundaries exist, and the angle of the magnetic field with respect to the axis of easy magnetization varies across the length of the specimen.

Characterization of torque gives the ability to directly probe the energetics of a sample in a magnetic field[15]. In a previous study we investigated the torque on a Ni-Mn-Ga single crystal specimen constrained with respect to bending in an external magnetic field. The torque magnitude varied by nearly a factor of 6 depending on the strain of the specimen, *i.e.* the twin domain fraction present in the specimen. We attempted to describe the torque with the change in magnetic energy as a function of the angle between the specimen and magnetic field. The magnetic energy was described assuming homogeneous magnetization in twin domains, but the torque could not be adequately described with the external field, demagnetizing field, and anisotropy energies but requires numerical, micromagnetic calculations, which is the objective of the present study.

II. MICROMAGNETISM

Micromagnetism is the numerical study of the energy contributions to the equilibrium magnetic structure of a material on a mesoscopic length scale. In other words, we seek the distribution of magnetic moments that minimizes the total energy with a resolution in the range of nanometers to

micrometers. We consider the following energies. (1) The exchange energy is the product of the exchange constant C_{ex}, with the square of the gradient of the magnetization, **M**, integrated over the sample volume:

$$E_{\mathrm{ex}} = C_{ex} \int_V |\nabla \mathbf{M}|^2. \quad (1)$$

(2) The magnetocrystalline anisotropy energy: Ni-Mn-Ga is uniaxial anisotropic with the anisotropy energy constant K_u :

$$E_{\mathrm{anis}} = \int_V K_u \sin^2\alpha \quad . \quad (2)$$

(3) The external field energy is the dot product of the external field vector **H** with the magnetization vector **M**. The external field energy is often referred to as the Zeeman energy:

$$E_{\mathrm{Z}} = -\mu_0 \int_V \mathbf{M} \cdot \mathbf{H}_{\mathrm{ext}}. \quad (3)$$

The constant μ_0 is the magnetic permeability of free space. (4) The internal field energy is the energy of the magnetic moments in the field created internally by the net magnetization in a magnetized specimen. The internal field is calculated using Poisson's equation, where the effective magnetic charge density ρ is found from the Laplacian of the magnetic potential U, expressed as $\Delta U = \rho$. The internal magnetic field, analogous to the electric field created by an electric potential, is given as $\mathbf{H}_{\mathrm{int}} = \nabla U$. The internal field energy is

$$E_{\mathrm{int}} = \frac{\mu_0}{2} \int_V |\nabla U|^2. \quad (4)$$

The effective magnetic field, **H**, at a point in a specimen is given as the first derivative of the energy with respect to magnetization:

$$\mathbf{H} = \frac{\delta E}{\delta M} = -\frac{2K_u}{M_S^2}(M_2 + M_3) + \frac{2C_{ex}}{M_S^2}\nabla \mathbf{M} - \mu_0 \nabla U + \mu_0 \mathbf{H}_{\mathrm{ext}}. \quad (5)$$

The effective field is the driving force for a change in magnetization which results in lower energy. Equation (5) assumes uniaxial magnetocrystalline anisotropy, where M_2 and M_3 are the magnetization components in Cartesian coordinates orthogonal to the axis of easy magnetization. M_s is the saturation magnetization. The relaxation process of the magnetization distribution in a ferromagnetic material is described by the Landau-Lifshitz equation[16]

$$\frac{d\mathbf{m}}{dt} = \gamma_0 \mathbf{M} \times \mathbf{H} - \frac{\alpha \gamma_0}{M_s} \mathbf{M} \times \mathbf{M} \times \mathbf{H}. \quad (6)$$

The constants α and γ_0 are the damping and gyromagnetic terms, respectively.

III. EXPERIMENTAL PROCEDURE

Single crystal specimen of Ni-Mn-Ga were grown with a modified Bridgeman-Stockbarger technique with an apparatus described in Ref.[17]. Specimen were grown with a nominal composition of $Ni_{50.5}Mn_{27.75}Ga_{21.75}$ (atomic percent); however, due to chemical segregation during growth there was a composition gradient across the crystal resulting in sections with different martensite structures at room temperature. Crystals were characterized in a Hitachi S3400 scanning electron microscope with energy dispersive x-ray spectroscopy (EDS, Oxford Instruments Energy$^+$ detector) and a Bruker D8 X-ray diffractometer with a Cu K_α source. Samples were cut with a Princeton Scientific WS-22 wire saw with a 50 µm diameter tungsten wire and polished using successively smaller grit SiC paper and then diamond slurries down to 1 µm diameter diamonds. The Ni-Mn-Ga sample tested had 10M structure with composition $Ni_{51.1}Mn_{25.7}Ga_{23.2}$ (atomic percent, as determined with EDS with accuracy atomic percent) and measured 16.46 x 5.02 x 3.62 mm^3 fully extended in the longest dimension and compressed in the intermediate dimension. The sample was subjected to constant magnetic fields $\mu_0 H$ from 50 to 1500 mT in a Varian Associates V3603 electromagnet. Once the samples had reached an equilibrium angle with the external magnetic field, a torque was applied as described below and the angular deflection was measured.

A cylindrical sample holder made from Teflon contained a groove to accommodate the sample (Figure 1). The sample holder had a diameter of 25.4 mm on which the sample was laid and a shaft with a smaller diameter of 9.53 mm which was press-fit into the inner bore of two ZrO_2 non-magnetic bearings and an E-5 optical encoder kit from US Digital with 5000 counts per revolution (Figure 2a). The ceramic bearings were placed in machined nylon between the pole pieces of an electromagnet (Varian Associates V3603). The optical encoder was fixed to the nylon with nylon screws.

The sample was placed in the sample holder and the magnetic field turned on to a set value. The sample turned to an equilibrium angle (γ_{eq}), this initial angle was measured by taking pictures using a Canon PowerShot A3000 digital camera and comparing the edge of the sample to a compass aligned in the field (Figure 2a) using the angle tool in ImageJ. We defined Cartesian coordinates on the sample such that the *x* direction coincided with the long edge of the sample and the rotation axis constituted the *z* direction. The sign of the coordinates was chosen such that the trace of the twin boundary plane (when moved through the coordinate origin) bisected the first quadrant of the *x*-*y* plane (Figure 1). The angle γ described the deviation of the magnetic field direction from the *x* direction. When the magnetic field was parallel to the *x* direction $\gamma = 0°$. The angle γ was positive when the sample was rotated clockwise or conversely a positive γ refers to a counter clockwise rotation of the magnetic field with respect to the sample coordinate system. The angular error was less than 0.5°.

The sample holder had a groove cut around the circumference where a string was wrapped around and extended to a spring force gauge (PCE Instruments) and pulley. The string transferred a displacement of the pulley to apply a tangential force to the sample holder and, thus, a torque to the sample. We manually recorded angle measurements with the optical encoder at regular intervals of applied torque. The optical encoder counts were compared to the measurement at γ_{eq} to calculate the total angle.

The sample was tested with microstructures containing different numbers of twin boundaries. The sample was manipulated manually to create the twin domain structure, which was characterized with optical images. We define the fully compressed state, i.e. when the crystallographic *c* direction is parallel to x in the entire sample, as the reference state with zero strain. When fully extended, i.e. when the crystallographic *c* direction is parallel to *y* in the entire sample, the sample had a strain of 6%. Since

the sample edge kinks by approximately 3.5° across the twin boundary, the strain could not be measured with a micrometer. The strain was found by determining the relative position of the twin boundary in the sample from a high resolution optical image in ImageJ. In the cases where the sample contained one twin boundary, the sample was placed on a glass slide and cast in a two-part polyamine epoxy. This constrained the sample, which froze twin boundaries, making it possible to test the sample at external magnetic fields greater than the switching field. Samples with two twin boundaries were tested without polyamine epoxy.

The sample was tested with one twin boundary at strains of 2.27%, 3%, and 3.92%. In the case where the sample contained two twin boundaries, two twin microstructures were tested, shown in Figure 1. One twin microstructure (Figure 1a) referred to as ABA had three twin domains where the central twin domain had *c* parallel to *y* and the other two domains had *c* parallel to *x*. The second microstructure, BAB, had the twin domain pattern reversed (Figure 1b). For this case, the sample was tested at a field of 75 mT at strain values of 2%, 3%, and 4%. Samples containing two twin boundaries had parallel faces on the ends, allowing strain measurement with a micrometer screw.

Experimental results are reported in terms of specific torque (Nm/m^3). We directly compare experimental and numerical results where the sample sizes vary.

IV. MICROMAGNETIC SIMULATION

Typically, the magnetization profile in a ferromagnetic sample displays large domains where the magnetization is slowly varying. These domains are usually of the order of a few hundreds of nanometers in size, and are separated by magnetic walls, and magnetic vortices. The core size of these sharp transition regions is of the order of a few nanometers. In order to carry out realistic micromagnetics simulations, it is therefore necessary to resolve numerically a broad range of length scales, spanning from the nanometer size magnetic walls and vortices to the macroscopic size of magnetic memories and hard drives. Moreover, the overall accuracy of the numerical simulation depends strongly on how well these local phenomena are resolved.

We solve the Landau-Lifshitz-Gilbert (LLG) equation (6) using the Gauss-Seidel Projection Method, developed in[18,19] . In this approach, only linear systems of the form

$$(\mathbf{I} - dt\backslash\Delta)\mathbf{M} = f \qquad (7)$$

must be solved where $\mathbf{I}$ is the identity matrix, Δ is the Laplacian, and f represents all lower order terms as defined in Ref.[19]. By carefully introducing the nonlinearity a posteriori, an unconditionally stable finite differences method for the LLG equation is obtained, which allows us to use relatively large time steps.

In the simulations, the spatial density of magnetic moments needed to be high enough in order to effectively capture the rotation of magnetic moments across Bloch walls between 180° magnetic domains, which are tens of nanometers wide in Ni-Mn-Ga[20]. Computation time increased significantly with increased number of magnetic moments, prohibiting the simulation of a sample with the same spatial dimensions (mm^2) as the sample used in the experiment. The parameters used in the micromagnetic simulation were as follows:

The real space dimensions of the simulated sample were 4 orders of magnitude smaller than the sample used in experiments. At 3% strain, the experimental specimen had dimensions 16.00 x 5.20 x 3.60 mm^3, and for simulations at 3% strain the specimen had dimensions 1.6 x 0.52 x 0.36 μm^3. The

simulation contained 384 magnetization vectors in the *x* dimension and 192 moments in the *y* dimension, resulting in magnetic moments spaced every 4.17 nm in the *x* dimension and every 2.83 nm in the *y* dimension.

The magnetic energy constants (magnetocrystalline anisotropy energy, exchange interaction energy, and saturation magnetization) are listed in Table 1.

Twin boundaries were defined such that the angle of the twin boundary crossed the sample at 45° in real space, consistent with the {101) type major twin boundaries seen in 10M Ni-Mn-Ga. The magnetocrystalline anisotropy energy and effective field due to the magnetocrystalline anisotropy energy were defined according to an axis of easy magnetization in different directions for neighboring twin domains. The A domain had the axis of easy magnetization in the *x* direction, while the B domain had the axis of easy magnetization in the *y* direction. The twin boundary constituted an abrupt change in the axis of easy magnetization.

Micromagnetic simulations were conducted at a constant external magnetic field and variable angle, γ, with respect to the sample. The discrete angles at which the code ran was changed depending on the twin domain structure in order to allow the code to find the same energy minima across multiple angle sweeps. An external magnetic field of 75 mT was applied to specimen with one, two, and 5 twin boundaries. The simulations ran for a fixed real time interval of 0.2 ns, during which 20,000 iterations of the minimization scheme ran. The equilibrium microstructure of magnetic moments was recorded along with the energy components described in section 2. This allowed us to view not only how each energy component changed as a function of angle, but also how the magnetic domain structure evolved.

The initial magnetic state of the sample was defined such that the component of the magnetic vector in each spatial dimension was equal. The normalized *x, y,* and *z* components of the magnetic vector each had an initial magnitude of $1/\sqrt{3}$, giving a total normalized magnetic vector magnitude of 1.

The two twin microstructures (Figure 1) which were experimentally tested with results were tested in the numerical simulations. All simulations, with one or two twin boundaries, had the twin boundaries oriented as in Figure 1. Coordinates and sense of rotation were as given in section 3 (Figure 1). For the ABA twin domain structure, the angle was swept in a loop from -γ = 0° to 80° and back to 0°. This sweep was considered one loop. When then back sweep did not show the same results as the forward sweep, a second loop was run with a narrower angle range around the angle for which the energy showed a minimum. This procedure was repeated until the back sweep coincided with the forward sweep.

V. EXPERIMENTAL RESULTS

The torque as a function of γ was tested for two different twin microstructures when the sample contained two twin boundaries. The equilibrium angle γ_{eq} depended equally on strain for the two twin microstructures (Figure 3a) while the maximum torque as a function of strain varied significantly (Figure 3b). At 2% strain and 50 mT, the BAB microstructure required 70% greater torque to rotate the sample than the ABA microstructure. This was the strain at which the greatest difference in torque occurred between the two microstructures. Away from 2%, the torque of the BAB and ABA microstructures were closer in magnitude. When the sample contained a single twin boundary, the equilibrium angle followed the same trend as the sample with two twin boundaries. The torque at 2% strain was larger than for the

two twin boundary conditions. At larger strain, the single twin boundary condition resulted in smaller torque, close to that of the ABA microstructure.

At low fields (*i.e.* <100 mT), the torque required to rotate the sample away from the equilibrium angle was symmetric about the equilibrium angle (Figure 4a). At larger fields, the torque required to rotate the sample in the clockwise direction did not follow a monotonic relationship. At fields larger than 250 mT, the torque first increased, reached a local maximum, and then decreased above approximately 15° away from γ_{eq}. When the torque passed the local maximum, the sample spun to a new location further from γ_{eq} with a similar torque value. At larger angle, the torque increased progressively. Upon decreasing the torque, the angle decreased until the torque reached a local minimum value. Upon further reduction of the angle, the sample spun back closer to γ_{eq} at a similar torque value (Figure 4b). The hysteresis shown in Figure 4b results from the experiment being torque-controlled. The torque-angle dependence between the two experimentally accessible branches is schematically indicated with the dotted black line. Thus, the angle exhibits a bifurcation. The angle is given in terms of $\Delta\gamma$, to plot the curves for different magnetic fields into one graph. This was not possible for plotting γ because the equilibrium angle changed as a function of external magnetic field (Figure 5a). The dashed lines in Figure 5a indicate the fields for which data was plotted in Figure 4a.

At 2% strain and magnetic fields larger than 250 mT the torque decreased with increasing magnetic field. The slope of the energy as a function of γ decreased, but never reached zero. There was no additional equilibrium angle. At 4% strain and fields greater than or equal to 250 mT, the sample experienced four equilibrium angles instead of two (which were 180 ° apart). The first equilibrium angle γ_{eq1} occurred in the same direction (negative γ) as the equilibrium angle at 2% and 3% strain. The other equilibrium angle γ_{eq2} occurred in the opposite direction (positive γ). The two unique equilibrium angles as a function of external magnetic field are given in Figure 5a. Each equilibrium angle had a similar dependence on the external magnetic field; they increased sharply up to 300-400 mT where the magnitude of the equilibrium angle reached a maximum at -55 ° (γ_{eq1}) and +55 ° (γ_{eq2}). Above 55 mT, the equilibrium angles were nearly constant up to 1500 mT. Each equilibrium angle had two-fold rotation symmetry about the sample rotation axis, but the equilibrium angles did not exhibit four-fold rotational symmetry.

VI. SIMULATION RESULTS

A. Two twin boundaries

Figure 6 shows the numerical results for the ABA twin domain structure with 3% strain. The energy as a function of γ for the converging third loop is shown in Figure 6a. The micromagnetic code calculated the exchange energy, magnetocrystalline anisotropy energy, stray field energy, and Zeeman energy. The variation in these individual energies (referred to their respective minimum values) are given as a function of γ in Figure 6b. The change in energy was plotted in order to view each energy on the same scale. The sum of anisotropy energy, exchange energy, and stray field energy is almost constant. The largest change in energy contribution came from the Zeeman energy. The change in Zeeman energy (blue solid circles in Figure 6b) very closely matched the total energy variation (Figure 6a).

The smallest and largest total energy occurred at γ = -30° and γ = -80°. The magnetic domain structure for these two field directions are shown in Figures 6c and 6d. The gray arrows indicate the average direction of magnetic moments in each domain. As -γ increased, the blue magnetic domains

grew domains grew to decrease the stray field energy in the A twin domains. As the blue domains grew, so did the green domain adjacent to it in the *B* twin domain, which increased the Zeeman energy. The central green domain shrank as γ approached 90°.

The total area of the blue and green domains as a function of γ is given in Figure 7a. As the area of the domains decreased, the stray field energy increased (Figure 6b). The stray field energy and area of demagnetizing magnetic domains were directly related. The magnitude of the net magnetization is given in Figure 7b. The net magnetization was correlated inversely to the Zeeman energy in Figure 6b. As the net magnetization increased, the Zeeman energy decreased.

Figure 8a gives the change in energy as a function of γ for the ABA and BAB microstructures. Again, the energies are plotted as differences to their respected minima to more easily compare the different energy contributions. The BAB microstructure resulted in a smaller total energy. The energy increased more quickly away from the minimum energy for the BAB microstructure. The simulation shows a larger torque for the BAB microstructure than for the ABA microstructure, as seen also in experiments. A quadratic function was fit to the energy values as a function of γ. The second derivative gives the slope of the torque as a function of γ, and is constant. This is similar to experimental data, which shows a constant slope of the torque near the equilibrium angle (Figure 4a). Experimental and simulation results for the slope of the torque for ABA, BAB and single twin microstructures are given in Table 2 for 75 mT and 3% strain. While the values are about a factor of 50 different between the experimental and simulated results, both show the same dependence of the torque on the twin microstructure. The difference in absolute values stems from the much smaller volume covered with the simulation.

The equilibrium magnetic structures for the ABA and BAB twin microstructures at 75 mT and γ = -30° are given in Figures 6c and 8b. The ABA microstructures contained 180° magnetic domain walls in both A and B twin domains, while the twin domains in the BAB microstructure were fully saturated. The BAB microstructure had a smaller total energy (5 kJ/m^3 compared to 20 kJ/m^3 for ABA), and the energy increased more quickly with changes in γ. Thus, the BAB microstructure required a larger torque to rotate.

B. Single twin boundary

The magnitude of the total energy (Figure 9a) and calculated torque were both close to and less than the energy and torque of the ABA microstructure at 3% strain and 75 mT external field. The magnetization of domain A, with axis of easy magnetization parallel to the long dimension of the sample, was normal to a small surface area. The magnetization in this domain created a small stray field and saturated at low fields (Figure 9b). The magnetization of the B domain was normal to a larger surface area. This domain did not saturate due to the larger stray field. Magnetic domains were present in domain B. The B domain magnetized such that there was no magnetization divergence at the twin boundary; no magnetic domains intersected the twin boundary since domain A was saturated.

At large fields, the torque was asymmetric about the equilibrium angle (Figure 4a). We calculated the energy for γ ranging from -90° to +90° (Figure 10a) for a sample at 2% strain with one twin boundary in an external magnetic field of 500 mT. The results of the simulation showed a decrease in the torque in the positive γ direction, as seen also in the experiment. The simulated data showed

another energy minimum, which was not seen in experiments at 2% strain. The simulated results overestimate the decrease in energy in the positive γ direction.

The change in magnetization perpendicular to the twin boundary was nearly symmetric about γ = 0° (Figure 10b). The magnitude of the change in each direction was similar, but larger when the external magnetic field was perpendicular to the twin boundary (γ = -45°) than parallel to the twin boundary (γ = +45°). In contrast, the divergence of the magnetization was not symmetric about γ = 0°. The divergence, which causes the stray field, was maximum when the field was parallel to the twin boundary, and had a local minimum when nearly perpendicular to the twin boundary.

The change in each energy term as a function of γ is given in Figure 10d. The total stray field energy was comparable in both directions, though slightly larger in the positive γ direction. The Zeeman energy was comparable, though slightly less in the positive γ direction. The magnetocrystalline anisotropy energy has two parabolas, with the parabola in the positive γ direction having a higher minimum energy. The minimum magnetocrystalline anisotropy energy occurs near the simulated equilibrium angle.

VII. DISCUSSION

The main experimental and numerical results are: (1) The magnetic torque on a Ni-Mn-Ga single crystal with equal fractions of A and B twin domains varies strongly with the twin microstructure; for example, a single crystal with a BAB microstructure experiences a much higher torque compared to a single crystal with an ABA microstructure. (2) The magnetic torque is asymmetric with respect to the direction of rotation; for example, a crystal with a single twin boundary experiences a monotonically increasing torque when turned in one direction and a bifurcated torque when turned in the other direction. We argue here that both effects have the same origin, namely the emergence of finite divergence of the magnetization at twin boundaries.

The derivative of the torque found from numerical simulations is approximately a factor of 50 less than the torque measured on a bulk single crystal specimen. We attribute this discrepancy to the difference in sample size, where the simulated sample is 4 orders of magnitude smaller in each dimension. The simulated results do show the same trend in maximum torque seen in experiments. At 3% strain, the BAB microstructure required the largest torque to rotate, the sample with a single twin boundary required the least, and the ABA microstructure required slightly more than the single twin and substantially less than the BAB microstructure. The numerical simulations provide a qualitative basis to analyze the results in terms of the magnetization of the twin domains.

The magnetization of twin domains is driven by the external field, but depends on the twin boundaries and crystal surface. The interfaces at the twin boundaries and crystal surfaces create a stray field if there is a divergence of magnetization. At crystal surfaces, any normal component of magnetization at the surface results in stray field energy. At the twin boundary, the stray field vanishes if the component of magnetization normal to the interface is constant across the interface. A discontinuity of the normal component of the magnetization increases the stray field energy.

In the BAB microstructure, the twin domains saturate fully while at the same angle and field magnitude the ABA microstructure does not. In the BAB microstructure, any 180° magnetic domain wall must pass through all three twin domains in order to maintain continuity across the twin boundaries because 180° boundaries in the A twin domain are parallel to the lateral crystal surfaces and span from

one twin boundary to the other. If continuity is not maintained, the divergence of magnetization creates a large stray field energy. Therefore, the formation of 180° magnetic domains would result in a relatively large volume of demagnetizing magnetic domains and, thus, an increase in Zeeman energy. In contrast, in the ABA microstructure, the 180° magnetic domain boundaries are perpendicular to the lateral surfaces. Therefore, these domain boundaries can extend from surface to surface without interacting with the twin boundaries in the B twin domain. The central B twin domain formed magnetic domains while not impacting the magnetic domain structure of the A twin domains. The blue magnetic domains in the A domains impact the magnetic domain structure in the intermediate B domain. The blue magnetic domains are positioned at the lateral surface of the A twin domain such that the enforced green magnetic domains in the B twin are minimal, and only one magnetic domain wall forms. For the ABA microstructure, the magnetic domains have more freedom to minimize the total energy compared to the BAB microstructure. Consequently, the total energy rises more quickly with deviation from the equilibrium orientation and the torque is larger for the BAB microstructure than for the ABA microstructure.

Simulation results revealed the interaction of the twin domain boundary with 180° magnetic domain walls when magnetic domain walls do not intersect the twin boundary. In the AB twin microstructure, the B twin domain has two green magnetic domains and four 180° magnetic domain walls (Figure 9b). The three 180° magnetic domain walls on the right are straight; they are perpendicular to the lateral surfaces and extend through the width of the B twin domain in a straight line. The leftmost green domain is curved. It is thin on the top such that it does not intersect the twin boundary, and gets wider toward the bottom where the twin boundary angles away from the 180° magnetic domain wall. The green domain in the ABA twin microstructure has a similar shape (Figure 6c). Both 180° magnetic domain walls curve such that the green magnetic domain shifts further away from the twin boundary near the top and bottom lateral surfaces. This constitutes a second, long range interaction between twin boundaries and magnetic domain boundaries in addition to the continuity requirement discussed above.

Besides the twin boundaries, the surfaces also add to the difference in magnetic domain structures. The direction of easy magnetization stands perpendicular to the lateral surfaces for the B twin domains and perpendicular to the end faces for the A twin domains. At 3% strain, the B domain has direction of easy magnetization normal to half of the lateral surfaces. In the ABA microstructure, the A domains have direction of easy magnetization normal to both end faces while the BAB microstructure the A domain does not interact with the crystal surface. The BAB microstructure has magnetization normal only to half of the lateral surfaces; the ABA microstructure has magnetization normal to half the lateral surfaces plus the end faces. If the twin domains are individually saturated (such as in Figure 8b for the BAB twin microstructure) and for an aspect ratio of 3:1, the BAB microstructure has magnetization normal to 3/8 the perimeter sample surface while the ABA microstructure has magnetization normal to 5/8 of the perimeter sample surface. Therefore, the free surfaces create an additional driving force for the formation of magnetic domains which is 67% larger for ABA microstructure compared with the BAB microstructure.

In the sample with the AB microstructure (single twin boundary), twin domain A saturates at low magnetic fields due to the small stray field. When saturated, the magnetization of the A domain is perpendicular to a small surface area, which results in small internal field. The B domain has 180° magnetic domains since the direction of easy magnetization is perpendicular to a larger surface area. The saturation of domain A forces the portion of domain B with direction of easy magnetization normal to the twin boundary to have no magnetic domain walls. This is the yellow area of the B domain under

the twin boundary in Figure 9b. This minimizes the divergence of magnetization at the twin boundary which minimizes the stray field energy. With decreasing strain, the volume fraction of the B domain decreases. The volume of the B domain forced to have no domain walls by the twin boundary (yellow area under the twin boundary) stays constant. Thus, as the strain decreases, the net magnetization of B increases. The net magnetization of the B domain is inversely proportional to the strain. As evidenced by the sample with two twin boundaries, larger net magnetization results in larger torque. In experiments, at 3% strain and above, the torque required to rotate the specimen with one twin boundary is smaller than for with the sample with the BAB microstructure. In contrast at 2% strain, the torque for the AB microstructure is similar to the BAB microstructure. The twin boundary causes a higher net magnetization of the B domain at 2% strain than at 3% strain; and this higher net magnetization results in a higher torque.

At 200 mT and above, the experimental torque is asymmetric about the equilibrium angle. The torque rises monotonically in the negative γ direction but goes through two inflections in the positive γ direction (Figure 4a). For magnetic fields larger than 500 mT, the torque goes through a local maximum and then through a local minimum. This causes a bifurcation in the torque-controlled experiment (Figure 4b). The simulated results for a sample with one twin boundary at 2% strain in an external field of 500 mT shows a decrease in energy in the positive γ direction (Figure 10). The total energy forms a biased double well with a lower minimum in the negative and a higher minimum in the positive γ direction. This double well potential corresponds to the experimental results of the sample with one twin boundary and 4% strain. In contrast, the experimental behavior of the sample with 2% strain corresponds to a potential as indicated by the black dotted line in Figure 10a. Thus, the calculations overestimate the energy depression in the positive γ direction.

The angular width of the bifurcation decreases with increasing external magnetic field above 500 mT. The equilibrium angle depends on the external magnetic field, and decreases in magnitude above 500 mT as well. The jump in angle in the clockwise direction is roughly twice the equilibrium angle. Considering the energy double well as the sum of two parabolas with minima in positive and negative γ, the width of bifurcation depends on the position of the minimum in the positive γ direction. As the external magnetic field increases, the position of the minimum increases. As the external field increases above saturation, the torque due to Zeeman energy goes to zero as the magnetization and magnetic field are parallel. The magnetocrystalline anisotropy and stray field energies increase toward a constant relationship with γ, where the stray field depends on $\sin(\gamma)$ and the magnetocrystalline anisotropy energy depends on $\sin(2\gamma)$. The increase of two energies and decrease of the other leads to the dependence of the angle jump on magnetic field magnitude, but more simulations are required to fully understand the contributions.

The equilibrium angle always occurs such that the component of the magnetic field perpendicular to the twin boundary is larger than the component parallel to the twin boundary. The change in magnetization perpendicular to the twin boundary is similar in the positive and negative γ directions (Figure 10b). The divergence of the magnetization perpendicular to the twin boundary is almost a factor 4 less when the magnetic field is perpendicular to the twin boundary than when it is parallel to the boundary (Figure 10c). Although the change in magnetization is similar for each case, the field parallel to the twin boundary (positive γ) creates a larger magnetization divergence and larger stray field energy than the field perpendicular to the twin boundary (negative γ). The smaller divergence in the positive γ direction contributes to the asymmetry of the double well.

The divergence in magnetization at the twin boundary results in effective positive magnetic charges at the twin boundary interface. These charges have a magnetic field which works to rotate the heads of the magnetic vectors away from the twin boundary. This increase in rotation results in larger magnetocrystalline anisotropy energy. This is why the magnetocrystalline anisotropy energy has a higher local minimum energy in the positive γ direction (Figure 10d). The rotation of the magnetization also rotates the magnetic vectors more parallel to the external magnetic field. Figure 10d shows the Zeeman energy is slightly less in the positive than in the negative γ direction. While the change in total stray field slightly increases in the positive γ direction, the divergence at the twin boundary results in a larger total increase in the magnetocrystalline anisotropy energy. If the divergence in magnetization was equal for both positive and negative γ, the sample at 2% strain would have two unique equilibrium angles. The angle of the twin boundary and difference in magnetization divergence for perpendicular or parallel orientation of the external magnetic field is the reason for the single equilibrium angle.

These results have direct implications on the design of actuators. For example, the BAB microstructure has the lowest total energy and largest torque for 3% strain and above. This suggests a twin domain microstructure might form which minimizes energy and maximizes torque. In linear actuators, torque leads to friction and loss of work output[21,22] and potentially to wear and fatigue[23]. The sample with a single twin domain had the largest torque at 2% sample strain, but the least torque at 3% strain. In an application where torque must be minimized, a single twin boundary is better at high sample strains. If possible, an actuator designer should target the ABA microstructure to minimize torque in a sample with an unconstrained end.

The magnetization in the A domain saturates at low fields. This makes the magnetization in the long dimension of the sample predictable. The twin domains in the BAB microstructure area saturates for low fields due to the stray field. A two-dimensional strain sensor would benefit from this microstructure. For sensing applications which sense with the magnetic flux, many twin boundaries will decrease the flux through the material[24]. The BAB microstructure, containing only two twin boundaries, is completely saturated for low fields due to the stray field. Targeting a microstructure which saturates at low fields but contains few twin boundaries would benefit sensing applications which sense with magnetic flux.

Kucza *et al.* proposed a microstructure in a bending sample with two twin domains and non-parallel twin boundaries[3]. Twin boundaries between the same two domains and non-parallel twin boundaries would result in large magnetization divergence at the boundary more parallel to the external field. It is possible that, small twin domains with direction of easy magnetization perpendicular to the field would form in order to minimize the stray field energy at the expense of increased Zeeman energy. This adds another variable to the complexity of modeling these actuators.

VIII. CONCLUSIONS

The magnetization of and, hence, torque on a single crystal Ni-Mn-Ga sample in a magnetic field and constrained with respect to bending depends on the strain and twin boundary structure. The twin boundary structure changed the torque by a factor of up to 1.7 for samples with equivalent strain and in the same external magnetic field. The results of numerical micromagnetic simulations qualitatively matched experimental results. Simulations predicted larger torque in the twin structure which showed larger torque in experiments. The simulations further revealed the microstructure with larger torque

had smaller total energy, which suggests a twin structure may form in an unconstrained sample which minimizes energy but maximizes torque.

Micromagnetic simulations showed that the twin boundary interface forces homogeneous magnetization in twin domains when the magnetization impinged on the twin boundary. In cases where the axis of easy magnetization was normal to the surface of the specimen, the twin domain split into multiple 180° magnetic domains. If the axis of easy magnetization was parallel to the lateral surface, the twin domain did not split into 180° magnetic domains if the neighboring twin domain was homogeneously magnetized. Although a homogenously magnetized domain is not energetically favorable according to the external field energy, the twin boundary interface forced this magnetic domain structure to avoid magnetization divergence at the interface. The divergence of magnetization at the twin boundary interface is maximum when the magnetic field is parallel to the twin boundary. The equilibrium angle always occurred such that the magnetic field made an angle less than 45° with the normal to the twin boundary. This was the case for samples containing one or two twin boundaries.

This study demonstrates a large dependence of the torque and magnetic energies on the twin microstructure. Thus, the design of MSMA-based actuators and sensors must include design of the twin microstructure and a strategy to maintain this twin microstructure over the duration of the operation of the device.

ACKNOWLEDGEMENTS

The authors would like to thank Eric Rhoads for single crystal growth and sample preparation, Danielle Nichols and Justina Freilich for help conducting experiments, Andrew Armstrong for shot-peening, Tammy Jackson for machining sample holders, and Juan Manuel Hernandez Calderon for helpful discussions. We thank Nanosteel for donation of equipment and the Micron School of Materials Science and Engineering and the National Science Foundation (project NSF-PFI 1500240) for partial financial support.

References

[1] O. Heczko, Materials Science and Technology **30**, 1559 (2014).

[2] P. Zheng, N. J. Kucza, C. L. Patrick, P. Mullner, and D. C. Dunand, Journal of Alloys and Compounds **624**, 226 (2015).

[3] N. J. Kucza, C. L. Patrick, D. C. Dunand, and P. Mullner, Acta Materialia **95**, 284 (2015).

[4] P. Mullner and K. Ullakko, Physica Status Solidi B-Basic Research **208**, R1 (1998).

[5] P. Mullner, V. Chernenko, M. Wollgarten, and G. Kostorz, Journal of Applied Physics **92**, 6708 (2002).

[6] R. C. O'Handley, *Modern Magnetic Materials* (Wiley, New York, 2000).

[7] R. C. O'Handley, S. J. Murray, M. Marioni, H. Nembach, and S. M. Allen, Journal of Applied Physics **87**, 4712 (2000).

[8] B. Kiefer and D. C. Lagoudas, Philosophical Magazine **85**, 4289 (2005).

[9] N. S. Kiselev, I. E. Dragunov, A. T. Onisan, U. K. Roessler, and A. N. Bogdanov, European Physical Journal-Special Topics **158**, 119 (2008).

[10] A. T. Onisan, A. N. Bogdanov, and U. K. Roessler, Acta Materialia **58**, 4378 (2010).

[11] N. N. Sarawate and M. J. Dapino, Journal of Applied Physics **101**, 123522 (2007).

[12] B. Kiefer and D. C. Lagoudas, Journal of Intelligent Material Systems and Structures **20**, 143 (2009).

[13] Y. W. Lai, N. Scheerbaum, D. Hinz, O. Gutfleisch, R. Schafer, L. Schultz, and J. McCord, Applied Physics Letters **90**, 192504 (2007).

[14] Y. C. Liang, H. Kato, M. Taya, and T. Mori, Scripta Materialia **45**, 569 (2001).

[15] A. Hobza and P. Müllner, Shape Memory and Superelasticity **3**, 139 (2017).

[16] E. M. Lifshits and L. D. Landau, Phys. Zeitsch. der Sow **8**, 153 (1935).

[17] D. Kellis, A. Smith, K. Ullakko, and P. Muellner, Journal of Crystal Growth **359**, 64 (2012).

[18] X. P. Wang, C. J. Garcia-Cervera, and E. Weinan, Journal of Computational Physics **171**, 357 (2001).

[19] C. J. Garcia-Cervera and Weinman E, IEEE Transactions on Magnetics **39**, 1766 (2003).

[20] D. I. Paul, W. McGehee, R. C. O'Handley, and M. Richard, Journal of Applied Physics **101**, 123917 (2007).

[21] T. Schiepp, V. Detkov, M. Maier, E. Pagounis, and M. Laufenberg, in *4th Int Conf on Ferromagnetic Shape Memory Alloys, ICFSMA*, edited by P. Müllner, and W. B. KnowltonBoise, ID, 2013), pp. 48.

[22] M. Chmielus, I. Glavatskyy, J.-U. Hoffmann, V. A. Chernenko, R. Schneider, and P. Muellner, Scripta Materialia **64**, 888 (2011).

[23] M. Chmielus, V. A. Chernenko, W. B. Knowlton, G. Kostorz, and P. Mullner, European Physical Journal-Special Topics **158**, 79 (2008).

[24] N. Gabdullin and S. H. Khan, Ieee Transactions on Magnetics **53**, 4900108 (2017).

[25] V. A. Chernenko, V. A. L'vov, P. Mullner, G. Kostorz, and T. Takagi, Physical Review B **69**, 134410 (2004).

[26] V. Runov and U. Stuhr, Journal of Magnetism and Magnetic Materials **323**, 244 (2011).

[27] A. Sozinov, A. A. Likhachev, and K. Ullakko, IEEE Transactions on Magnetics **38**, 2814 (2002).

Tables

TABLE I. Numeric values of magnetic energy constants for 10M Ni-Mn-Ga for micromagnetic simulations

Energy Term	**Value**	**Reference**
Saturation magnetization (M_s)	0.61 Tesla	[25]
Exchange interaction energy (C_{ex})	6×10^{-12} J/m	[26]
Magnetocrystalline anisotropy energy (K_u)	2.45×10^5 J/m^3	[27]

TABLE II: Derivative of the specific torque as a function of γ near the equilibrium angle. The experimental results showed nearly linear (constant slope) increase in torque close to the equilibrium angle. A quadratic function was fit to the simulated energy. The second derivative of the quadratic function is a constant which gives the rate of change of the torque with increasing γ.

Twin boundary structure (3% strain, 75 mT)	Derivative of specific torque: Simulation ($Nm/m^3/°$)	Derivative of specific torque: Experimental Results ($Nm/m^3/°$)
One twin boundary	4.00	218
Two twin boundaries – ABA	4.86	235
Two twin boundaries – BAB	8.79	300
Five twin boundaries	7.47	

Figures

Figure 1

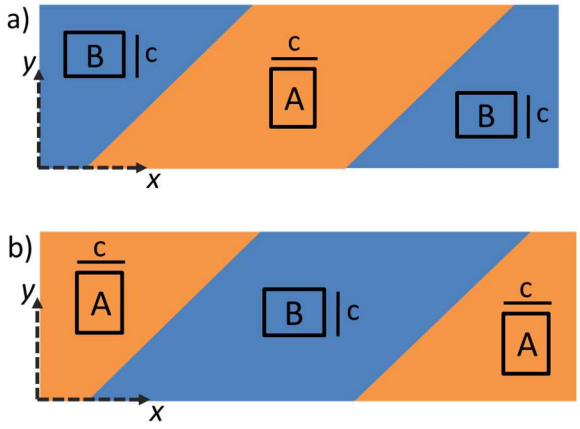

FIG. 1: A sample containing two twin boundaries may have either microstructure, denoted by "ABA" (a) or "BAB" (b). The axis of easy magnetization is parallel and perpendicular to the lateral surface in twin domains A and B, respectively.

Figure 2

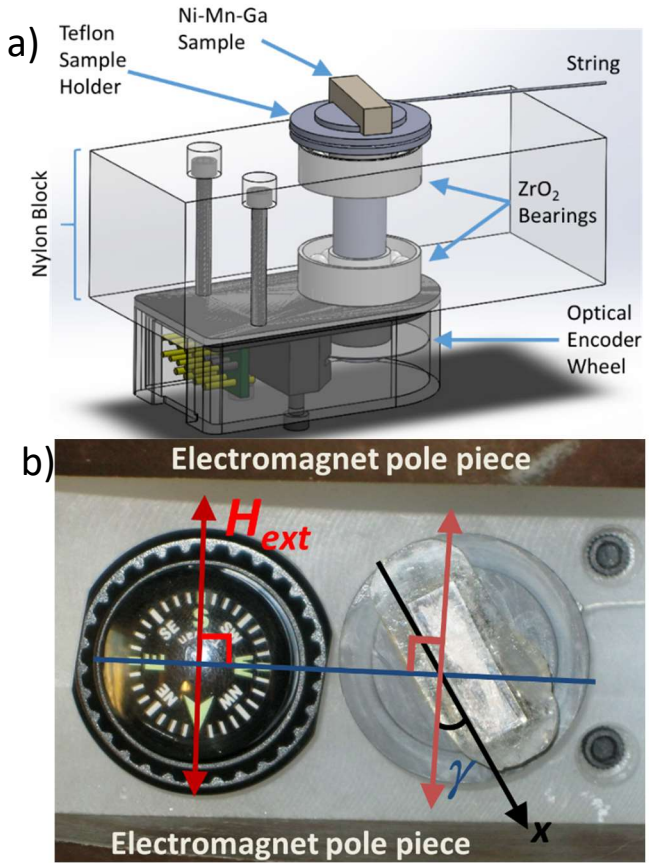

FIG. 2: The platform of the experimental apparatus was made from a nylon block which was press fit in between the pole pieces of the electromagnet. (a) Two ceramic bearings were press fit into the nylon block. The inner diameters of the bearings guided the shaft of the Teflon sample holder into the optical encoder wheel, which was attached with a set screw. The Ni-Mn-Ga sample was laid in a groove on the sample holder. A groove was cut around the circumference of the sample holder, into which a string was tied and wrapped to apply the torque. (b) The initial angle, γ, of the sample to the external magnetic field was determined by comparing the edge of the sample to the angle of a compass deflected by the magnetic field.

Figure 3

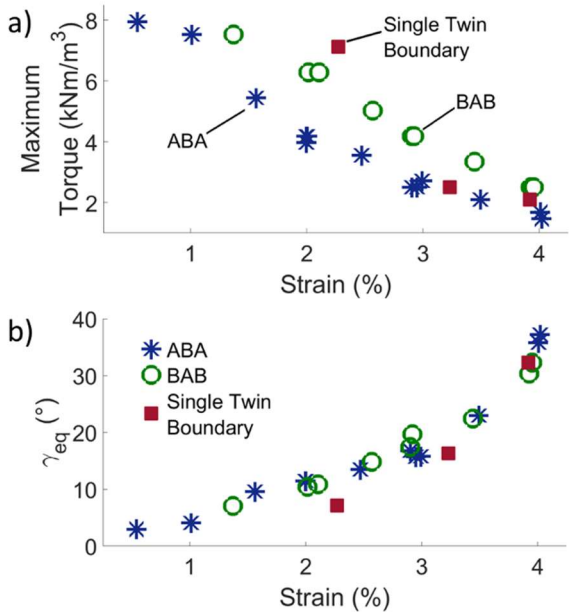

FIG. 3: Experimental results for the maximum specific torque as a function of strain for a single twin as well as ABA and BAB twin microstructures at an external field of 50 mT (a). The equilibrium angle is shown as a function of sample strain (b). Results for the ABA and BAB microstructures are denoted with blue stars and open green circles, respectively. Results for samples with a single twin boundary are shown in solid maroon squares.

Figure 4 –

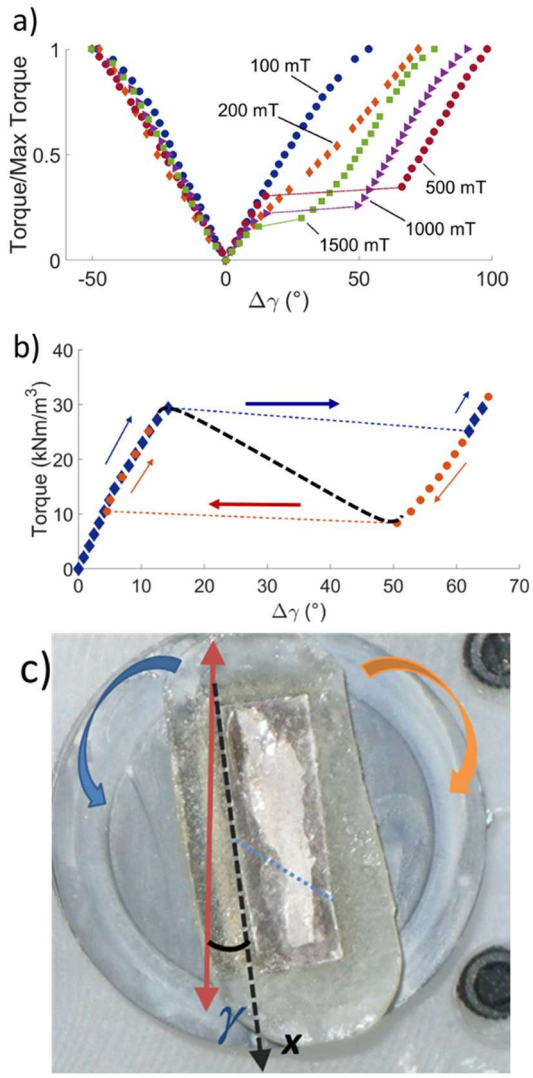

FIG. 4: Experimental data for the normalized torque as a function of the change in γ from the equilibrium angle for a sample with one twin boundary at 2% strain (a). Data is given for 100 mT, 200 mT, 500 mT, 1000 mT, and 1500 mT in both the positive and negative g directions. Positive γ is in the clockwise direction, and negative γ is the counterclockwise direction. For magnetic fields above 200 mT, the torque decreased after ~15° rotation in the clockwise direction. The sample holder spun to a new angle, hence the abrupt jump in angle. The decrease in torque is shown in (b) for 500 mT. The jumps in angle represent show the bifurcation, since the stimulus to the sample was torque and there are multiple possible angles at the same torque. The dotted black line approximates the torque in the intermediate angle range. The sample for 2% strain is shown, containing the location of the twin boundary (dashed blue line) at the equilibrium angle at a magnetic field of 50 mT(c).

Figure 5

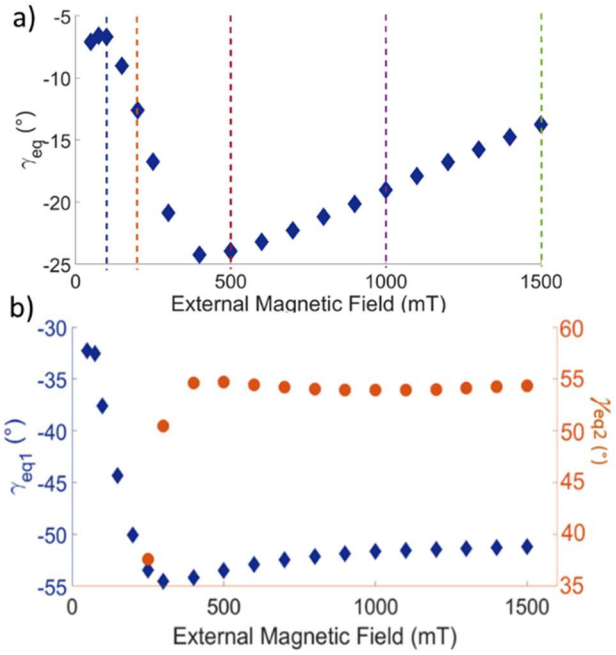

FIG. 5: Experimental results for the equilibrium angle as a function of external magnetic field for a sample with one twin boundary at 2% strain (a) and 4% strain (b). Dashed lines indicate the equilibrium angles for the fields plotted in Figure 4a. At fields 250 mT and larger, two unique equilibrium angles existed for the sample at 4% strain.

Figure 6

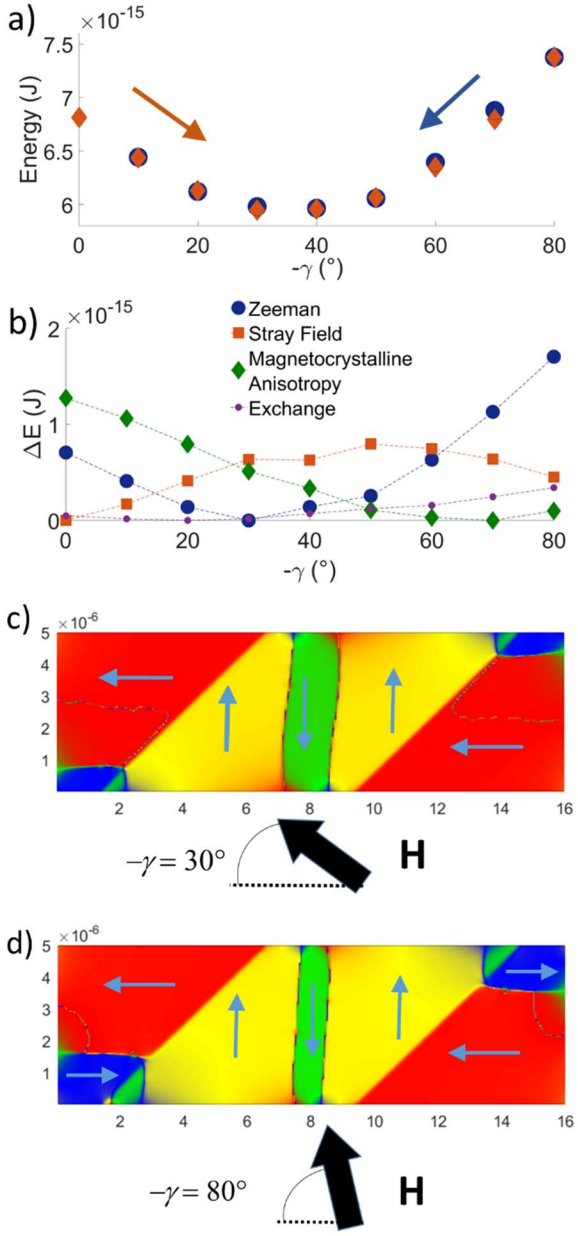

FIG. 6: Simulation results for the magnetic energy as a function of angle is given for the ABA twin structure at a strain of 3%. The total energy is given as a function of γ- (a) and separated in its contributions in (b) as a difference to its respective minimum value. The equilibrium magnetic domain structure is shown for -γ = 30 ° (c) and -γ = 80 ° (d).

Figure 7

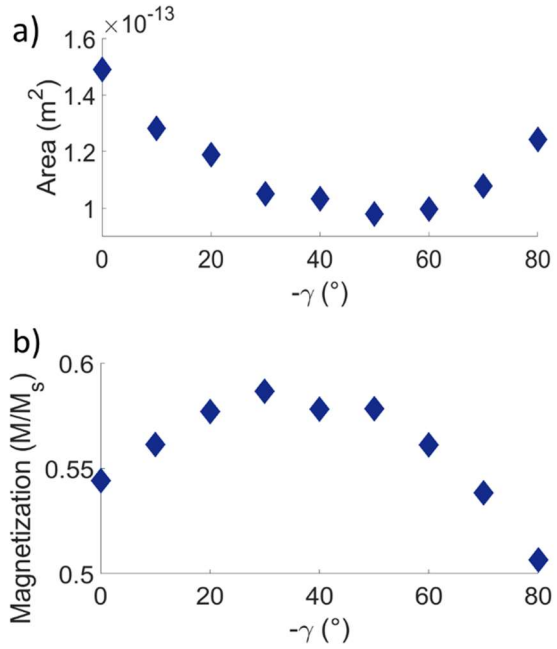

FIG. 7: Simulation results for the ABA twin microstructure giving the total area of the blue and green magnetic domains (a) and the net magnetization (b) plotted against -γ.

Figure 8

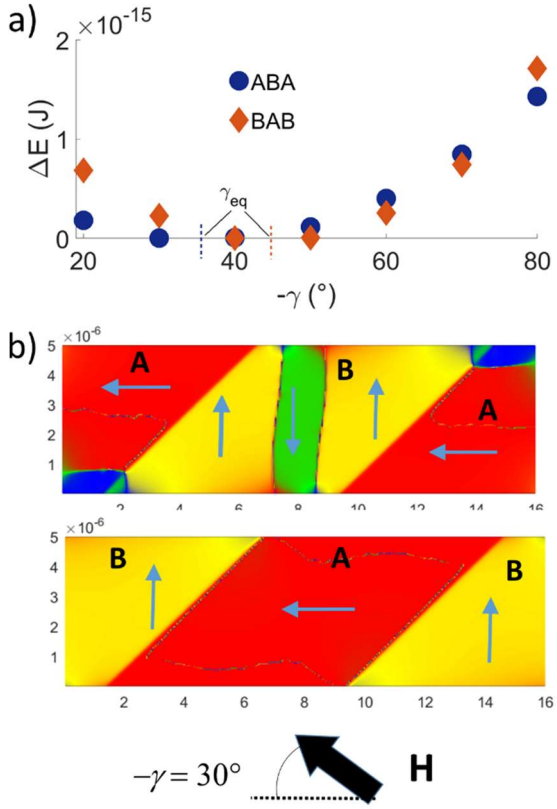

FIG. 8: Simulated results for the change in total energy with respect to the minimum energy is given as a function of -γ for the ABA and BAB microstructures (a) along with the equilibrium magnetic domain structure at an angle of $-\gamma$ = 30° (b). The ABA microstructure (top) has 180° magnetic domains in both twin domains, while the BAB microstructure (bottom) has fully saturated domains. The simulated samples are both at 3% strain with an external magnetic field of 75 mT.

Figure 9

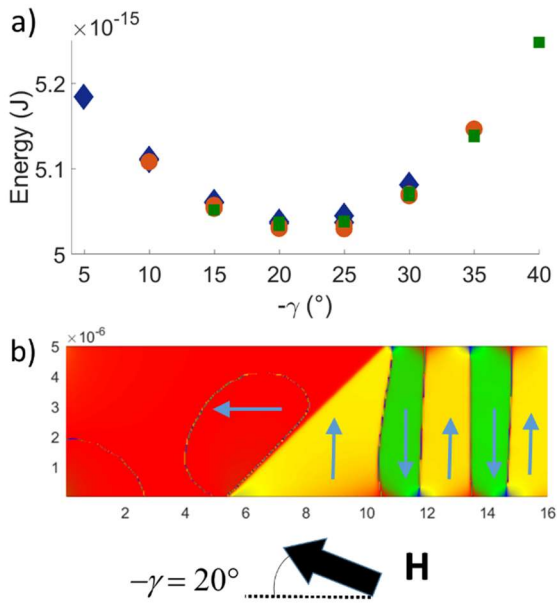

FIG. 9: The total energy is given as a function of -γ (a) along with the equilibrium magnetic structure at the lowest energy for a sample at 3% strain and 75 mT with one twin boundary (a). The magnetic domain structure at -γ = 20° (b) shows a fully saturated A twin domain while the B twin domain has two demagnetizing 180° magnetic domains which extend from lateral surface to lateral surface without intersecting the twin boundary. To avoid intersecting the twin boundary, the outermost left 180° magnetic domain curves to the right.

Figure 10

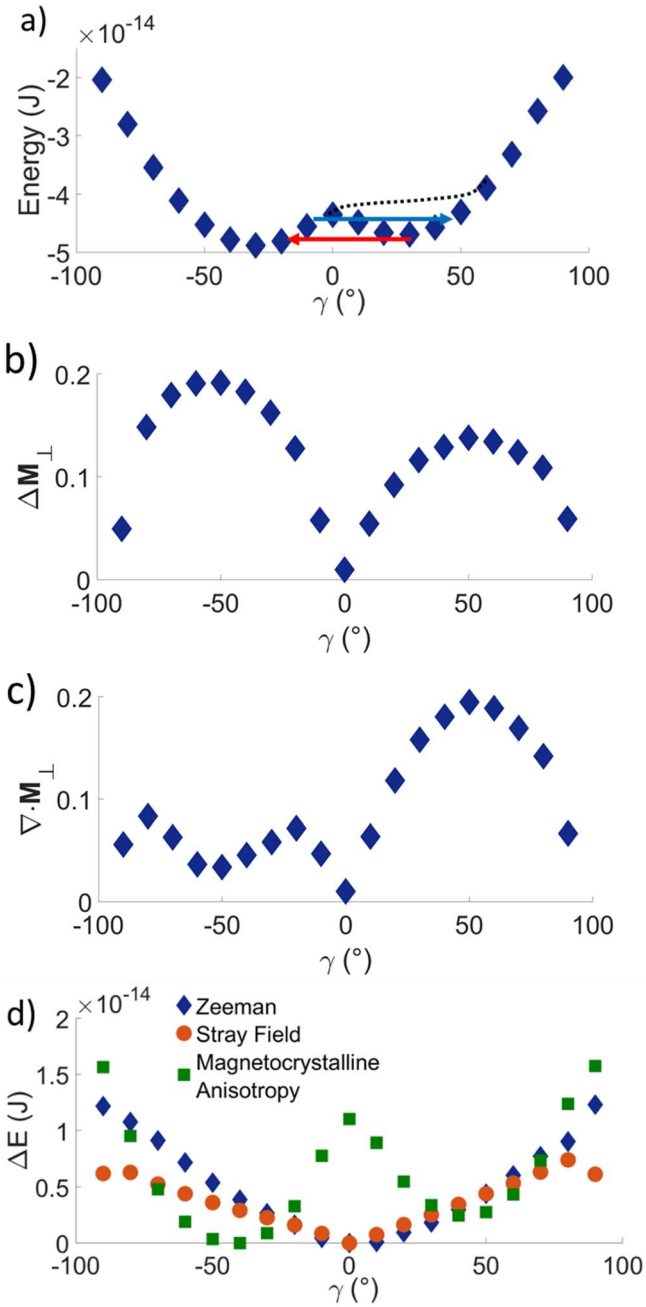

Figure 10: Simulated results for the energy as a function of γ at 2% strain and 500 mT for a sample with one twin boundary (a). The arrows mark the bifurcation of the stable position under torque as displayed in Figrue 4b. The change in magnetization normal to the twin boundary (b) and the divergence of the magnetization normal to the twin boundary (c) are given as a function of γ. The change in energy from the minimum for each individual energy component is given as a function of γ (d).